



## Research article

# 2D Ni<sub>2</sub>P/N-doped graphene heterostructure as a Novel electrocatalyst for hydrogen evolution reaction: A computational study

Amin Esmaili<sup>a</sup>, Farhad Keivanimehr<sup>b</sup>, Maryam Mokhtarian<sup>b</sup>, Sajjad Habibzadeh<sup>b,\*</sup>, Otman Abida<sup>c</sup>, Mohammadreza Moghaddamian<sup>d</sup>

<sup>a</sup> Department of Chemical Engineering, School of Engineering Technology and Industrial Trades, College of the North Atlantic - Qatar, Doha, Qatar

<sup>b</sup> Surface Reaction and Advanced Energy Materials Laboratory, Chemical Engineering Department, Amirkabir University of Technology (Tehran Polytechnic), Tehran, Iran

<sup>c</sup> African Sustainable Agriculture Research Institute (ASARI), Mohammed VI Polytechnic University (UM6P), Laayoune, 70000, Morocco

<sup>d</sup> Department of Chemical Engineering, Mahshahr Branch, Islamic Azad University, Mahshahr, Iran

## ARTICLE INFO

## Keywords:

Density functional theory  
Hydrogen evolution reaction  
Ni<sub>2</sub>P  
Graphene  
van der waals

## ABSTRACT

The main prerequisite for designing electrocatalysts with favorable performance is to examine the links between electronic structural features and catalytic activity. In this work, Ni<sub>2</sub>P as a model electrocatalyst and one of the most potent catalysts for hydrogen evolution reaction (HER) was utilized to develop various Ni<sub>2</sub>P and carbon-based (graphene and N-doped graphene) heterostructures. The characteristics of such structures (Ni<sub>2</sub>P, graphene, N-doped graphene, Ni<sub>2</sub>P/graphene, and Ni<sub>2</sub>P/N-doped graphene), including binding energies, the projected density of states (PDOS), band structure, charge density difference, charge transfer, Hirshfeld charge analysis, and minimum-energy path (MEP) towards HER were calculated and analyzed by density functional theory (DFT) approach. The coupling energy values of hybrid systems were correlated with the magnitude of charge transfer. The main factors driving a promising water-splitting reaction were explained by the data of PDOS, band structures, and charge analysis, including the inherent electronegativity of the N species alongside shifting the Fermi level toward the conductive band. It was also shown that a significant drop occurs in the HER energy barrier on Ni<sub>2</sub>P/graphene compared to the pristine Ni<sub>2</sub>P due to N doping on the graphene layer in the Ni<sub>2</sub>P/N-doped graphene heterostructure.

## 1. Introduction

Due to the higher global energy demands and severe environmental impacts of fossil fuels, clean and renewable energies are required to replace conventional fuels for extensive use on a global scale [1–4]. Hydrogen plays a crucial role as an alternative energy-carrying element in the forthcoming energy systems due to its high energy density and eco-friendly properties [5–7]. Hydrogen generation via water electrolysis is among the cleanest and most effective techniques with numerous advantages [8]. The hydrogen evolution reaction (HER) is the critical reaction of water electrolysis that requires an efficacious electrocatalyst to improve hydrogen

\* Corresponding author.

E-mail address: [Sajjad.habibzadeh@mail.mcgill.ca](mailto:Sajjad.habibzadeh@mail.mcgill.ca) (S. Habibzadeh).

<https://doi.org/10.1016/j.heliyon.2024.e27133>

Received 22 August 2023; Received in revised form 22 January 2024; Accepted 23 February 2024

Available online 9 March 2024

2405-8440/© 2024 Published by Elsevier Ltd.

This is an open access article under the CC BY-NC-ND license

(<http://creativecommons.org/licenses/by-nc-nd/4.0/>).

generation efficacy [9–11]. The existing modern HER electrocatalysts are typically based on Pt-containing materials or other noble metals that are usually costly due to their rare resources and limited supply [12,13]. Therefore, there is a considerable need to design non-noble metal HER catalysts that can be practically produced on large scales at low prices.

With that in mind, transition-metal phosphides (TMPs) have recently attracted much attention due to their high catalytic activity, long-term durability, good conductivity, and low price [14,15]. Among the developed TMP catalysts, Ni<sub>2</sub>P has reportedly shown several promising properties as an HER electrocatalyst as it possesses: (i) a poor "ligand effect" owing to Ni–P bonds that accelerate the dissociation of hydrogen molecule; (ii) the "ensemble effect" of P that reduces the concentration of the active sites on the surface and prevents the catalyst toxicity due to the high coverage; and (iii) the P sites provide strong bonding to the generated hydrogen molecule [16]. Although pristine Ni<sub>2</sub>P demonstrates remarkable HER performance, one of its main drawbacks is the high overpotential (>150 mV), resulting in weaker HER performance in strict acidic electrolytes compared to the HER activity of the standard, high-tech Pt/C electrocatalyst [17].

On the other hand, the excellent conductivity and high surface area of carbon substances make them ideal candidates for HER. Some chemically substituted carbon atoms with heteroatoms (e.g., N, B, P, S, etc.) may lead to the modulation of physicochemical specifications of the carbon for obtaining additional active sites [18–20]. Among various candidates for doping with carbon substances (e.g., graphite, graphene, carbon nanotube, carbon fiber, etc.), nitrogen can be an outstanding option as it shows an inherently greater electronegativity than carbon [21,22]. N-doped carbon nanotubes with vertical alignment have reportedly shown superior catalytic activities relative to Pt [23]. According to Qu et al. (2010), the catalytic current at the N-doped graphene (NG) electrode is three orders of magnitude higher compared to that of the Pt/C electrode across a wide-ranging potentiality [24]. In addition, NG was reported to display an enhanced HER activity compared to inherent graphene because of the modulation of its electronic constructs [25]. Nonetheless, the HER activity of NG is far less than that of standard noble metal catalysts and high-tech transition metal compounds.

Moreover, van der Waals (vdW) heterostructures, consisting of a monolayer placed over another monolayer or a few-layer crystal, are suggested to be the modulators of the electrical and optical features of 2D materials [26–28]. Recent studies also indicated the effectiveness of such heterostructures due to their promising electrocatalytic performance [29]. Besides, defect-free basal planes are inactive against any catalytic reactions, especially in 2D layers [29]. According to other reports, however, the intrinsic electrocatalytic activity of each layer toward particular reactions can drastically change by creating heterostructures in which the atomic layers are located one above the other with a different atomic layer. This may even result in basal plane activity or render it inactive. This is mainly due to the impact of the in-built electric field among the metallic layers or sublayers [30–32]. Consequently, the VdW heterostructure (heterojunction), which has been established through experimentation, has been of considerable interest in the field of electrocatalysts. For instance, a recently published experiment-based investigation indicated that stacked VdW vertical heterostructures of catalytic graphene (G) and inactive hexagonal Boron Nitride (hBN), (hBN/graphene (G)) could be activated by vdW stacking [33], and these heterostructures are capable of acting as effective catalysts for HER. Similarly, such an impact has been detected from graphene/MoS<sub>2</sub> vertical heterojunctions, in which the photo-electrocatalytic specifications of the VdW heterostructure with graphene on MoS<sub>2</sub> show the utmost activity for HER in comparison to each layer alone as well as MoS<sub>2</sub> on graphene [34]. Moreover, carbon and N-doped carbon materials such as CuS/Graphene could reach excellent electronic properties with other 2D structures [35], Ni<sub>2</sub>P/N- and S-doped graphene (NSG) nanosheets [36], NiCoP/N-doped carbon (NC) [37], RuMo/NC [38], WSe<sub>2</sub>/multiwalled carbon nanotube (MWNT) [39], ZnIn<sub>2</sub>S<sub>4</sub>/g-C<sub>3</sub>N<sub>4</sub> [40], Ni<sub>2</sub>P/N-doped reduced graphene oxide (N-RGO) [41], and WS<sub>2</sub>/C<sub>2</sub>N, the design of which is usually conducted by successive layer-by-layer deposition [42].

Despite several previous studies on the impacts of the TMPs 2D structures (particularly Ni<sub>2</sub>P) on the catalytic performance of graphitic materials, few systematic investigations help to comprehensively understand the reaction mechanism and the electronic properties of the structures. To the best of the authors' knowledge, until now, there has been no study on this elaborated approach to VdW structures based on atomic layers. Moreover, tuning their HER properties to compare them with standard metal/metal oxide-based catalysts is necessary.

To address the abovementioned concern, the DFT calculation was employed periodically to examine the Ni<sub>2</sub>P/graphene and Ni<sub>2</sub>P/NG VdW heterostructures in this study. The goal was to establish a basal physical depiction of these heterostructures by the interconnection of Ni<sub>2</sub>P with graphene and an NG monolayer to investigate the interface structure and electronic properties. The geometrical structures, interfacial binding energy, band structure, electronic structure, and projected density of state (PDOS) were deeply investigated, along with the electron density difference (EDD) and Hirshfeld charges on various atoms. In addition, the impacts of graphene and NG were examined on the energy barrier of the reaction coordinate of water splitting using the nudged elastic band (NEB) theory. Moreover, a new perspective is presented to prepare a non-noble metal electrocatalyst, which can be applied in the electrocatalytic splitting of water.

## 2. Calculation method

In this study, we optimized the system geometry and calculated the electronic structure using the DFT approach. To reduce the lattice mismatch of the Ni<sub>2</sub>P and graphene layer lower than 2.5%, we employed a model containing a 7 × 7 single graphene layer with 98 carbon atoms for the graphene and NG surfaces to conform to a 3 × 3 pristine Ni<sub>2</sub>P. The vacuum space along the z direction is adjusted to around 20 Å to prevent interactions between the periodic slabs. There were entirely relaxed atoms and cells for the Ni<sub>2</sub>P and graphene-based materials. The following formulation was applied to calculate the binding energies of the composites [43]:

$$E_b = E_{\text{Ni}_2\text{P}/\text{Graphene material}} - E_{\text{Ni}_2\text{P}} - E_{\text{Graphene material}} \quad (1)$$

Where,  $E_{\text{Ni}_2\text{P}/\text{Graphene material}}$ ,  $E_{\text{Ni}_2\text{P}}$  and  $E_{\text{Graphene material}}$  represent the total energy of Ni<sub>2</sub>P/graphene (or Ni<sub>2</sub>P/NG), pristine Ni<sub>2</sub>P, and graphene (or NG) monolayers, respectively. A negative Eb represents a stable adsorption structure. All the calculations were employed using the CASTEP code [44]. The generalized gradient approximation (GGA) was used to describe the Perdew-BeckeErnzerhof (PBE) for the exchange-correlation function [45]. A poor VdW interaction between the adjoining layers of the heterostructure was examined using the DFT-D2 functional with the Grimme correction [46]. All the estimations were performed by considering spin-polarization.

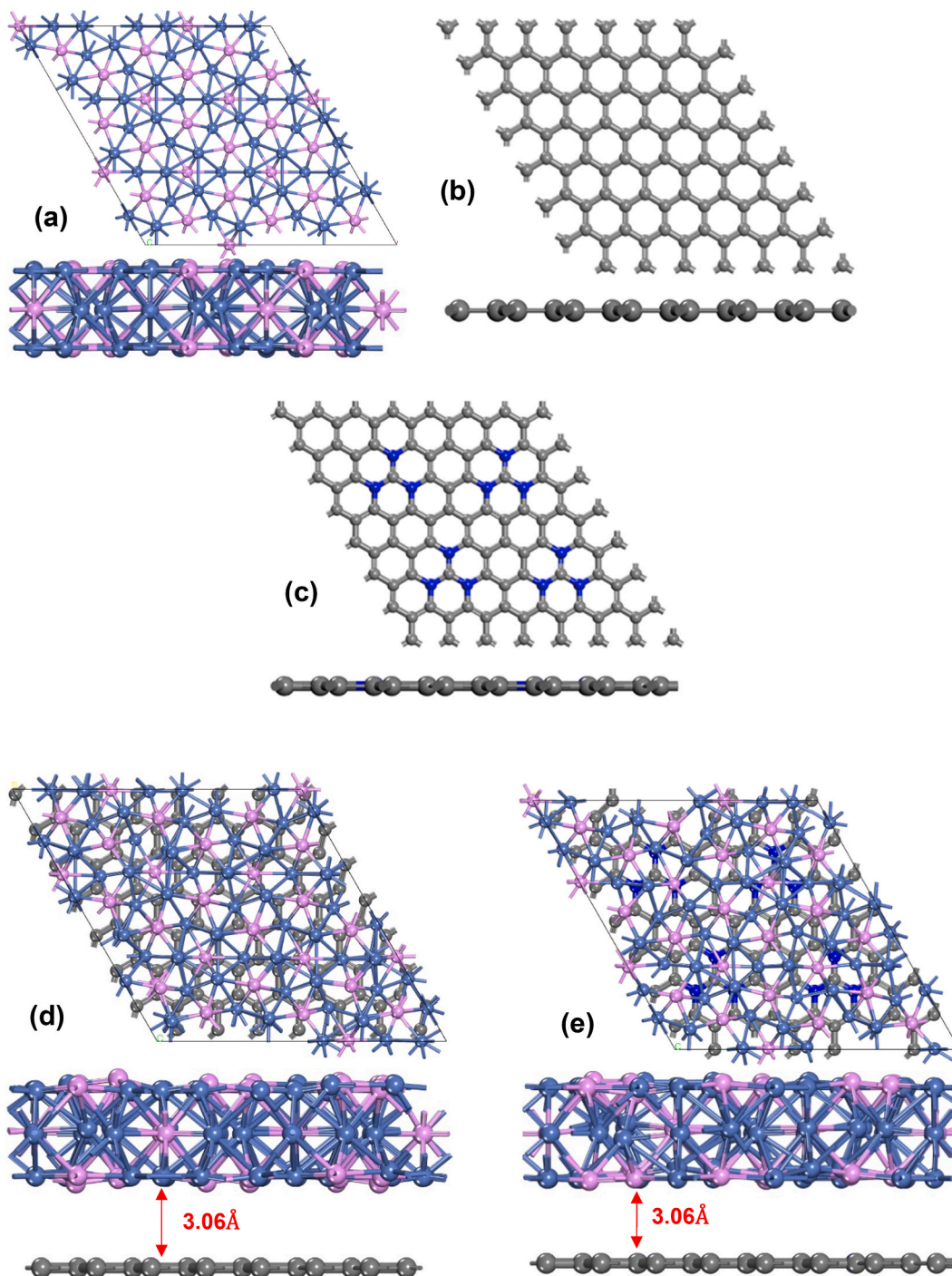


**Fig. 1.** The top and side views of the most stable configurations of (a) pristine Ni<sub>2</sub>P, (b) graphene monolayer, (c) NG monolayer, (d) Ni<sub>2</sub>P/graphene heterostructure, and (e) Ni<sub>2</sub>P/NG heterostructure. The purple, pink, gray, and blue balls represent nickel, phosphorus, carbon, and nitrogen atoms, respectively. (For interpretation of the references to color in this figure legend, the reader is referred to the Web version of this article.)

The electron-ion interaction in reciprocal space was described using the plane-wave ultrasoft pseudopotential method, which accounted for the ionic cores of Ni-3d<sup>8</sup>4s<sup>2</sup> and P-3s<sup>3</sup>3p<sup>2</sup>. The Self-consistent Field (SCF) is considered to be converged while the electronic energy changes at 10<sup>-6</sup> eV/atom. For geometric optimization and energy calculation, the setting of convergence benchmarks was as follows: (a) a maximum force tolerance of 0.01 eV/Å, (b) an energy tolerance of 10<sup>-5</sup> eV/atom, (c) a maximum displacement tolerance of 0.001 Å, and (d) a plane wave cutoff energy of 450 eV. Additionally, a Monkhorst Pack mesh of 3 × 3 × 1 k-points was used to sample the Brillouin zone and a finer mesh with 5 × 5 × 1 k-points was applied to calculate the PDOS.

All reactions are performed at the vacuum condition. The quadratic synchronous transit (QST)/linear synchronous transit (LST) and nudged elastic band (NEB) approaches were used to determine the MEP for each step in the reaction [47,48]. Vibrational frequencies, portraying an imaginary frequency over the potential energy surface (PES), confirmed the nature of the transition states. The simulation would stop when the orthogonal force reached 0.01 eV/Å. The MEP designated the topmost image as the transition state (TS). For each step in the reaction, the activation energy barrier ( $\Delta E_{Activation}$ ) was estimated as follows [49,50]:

$$\Delta E_{Activation} = E_{TS} - E_{IS}$$

The charge density difference ( $\Delta\rho$ ) is calculated by using the following equation [51]:

$$\Delta\rho = \rho_{Ni_2P/Graphene\ material} - \rho_{Ni_2P} - \rho_{Graphene\ material} \quad (2)$$

Where  $\rho_{Graphene\ material}$ ,  $\rho_{Ni_2P}$  and  $\rho_{Ni_2P/Graphene\ material}$  are the charge densities of graphene monolayer (or NG), pristine Ni<sub>2</sub>P, and Ni<sub>2</sub>P/graphene (or Ni<sub>2</sub>P/NG) heterostructure, respectively.

### 3. Results and discussion

#### 3.1. Optimizing the structures and binding energies

Fig. 1 shows the configuration of the structures with utmost stability. The supercells of catalytic models were made by the optimization of graphite ( $a = b = 2.467$  Å,  $c = 8.685$  Å) and Ni<sub>2</sub>P ( $a = b = 5.164$  Å,  $c = 4.656$  Å). In particular, the 7 × 7 supercell of graphene (98 C atoms) with  $a = b = 17.274$  Å and the 3 × 3 supercell of Ni<sub>2</sub>P (001) (90 Ni atoms and 45 P atoms) with  $a = b = 17.618$  Å were used for making the computed models (Fig. 1 a and b). Regarding the graphene structures, NG could preserve the planate shape of

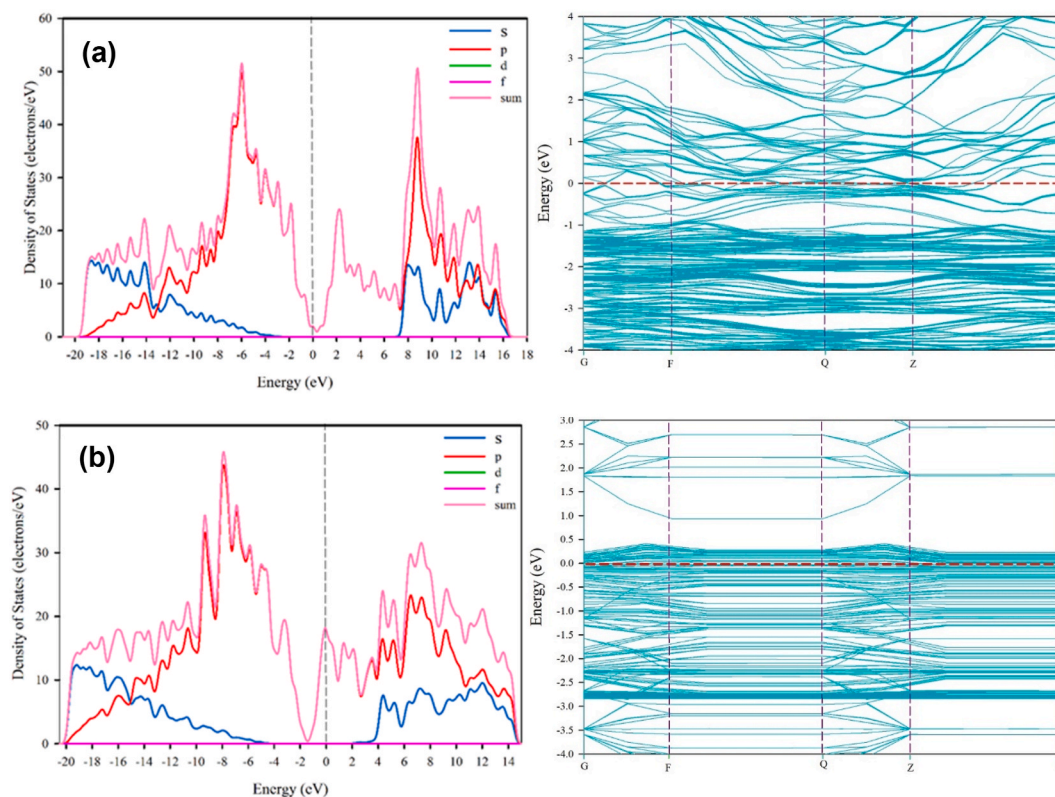


**Fig. 2.** Estimated PDOS and equivalent band structures for (a) Pristine Ni<sub>2</sub>P; (b) Graphen monolayer; (c) N-doped graphene monolayer; (d) Ni<sub>2</sub>P/graphene heterostructure; and (e) Ni<sub>2</sub>P/NG heterostructure with PBE functional. The Fermi level is allocated at 0 eV (the green dashed line). (For interpretation of the references to color in this figure legend, the reader is referred to the Web version of this article.)



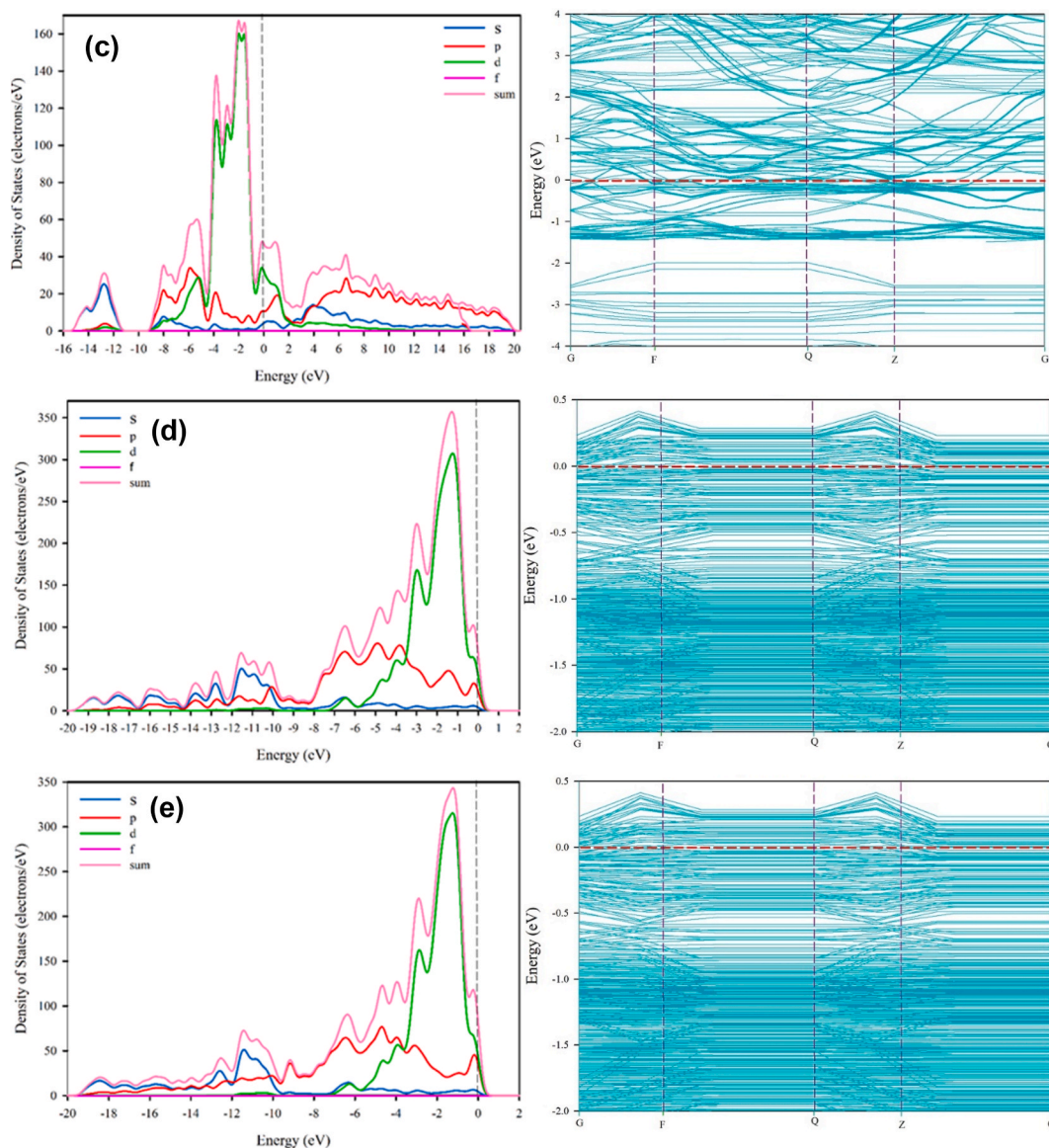


Fig. 2. (continued).

intact graphene when it was fully relaxed. In comparison to the C–C bond length of 1.42 Å in intact graphene, which corresponds to the experimentally obtained value [52,53], the C–N bond length was obtained at 1.389 Å for NG, which is in good accordance with values reported in previous studies [54,55]. The lengths of the Ni–Ni and Ni–P bonds were computed at 2.656 Å and 2.204 Å, both of which fall into 2% of the values obtained experimentally [56]. The mismatch (2%) between the  $7 \times 7$  supercell of graphene (17.274 Å) and  $3 \times 3$  supercell of Ni<sub>2</sub>P (001) (17.618 Å) is proper for forming the heterostructure produced by graphene and Ni<sub>2</sub>P (001).

In the present study, the Ni<sub>2</sub>P/graphene and Ni<sub>2</sub>P/NG heterostructures are constructed by placing a single-layer Ni<sub>2</sub>P at the top of monolayer graphene and NG slabs. The minimum distance between the Ni<sub>2</sub>P nanosheet and the graphene surface is 3.24 Å; meanwhile, the minimum distance between the Ni<sub>2</sub>P nanosheet and the NG surface is 3.06 Å. There was a poor interaction between Ni<sub>2</sub>P and graphene-based layers that belonged to the VdW interaction. Structural distortions were absent on Ni<sub>2</sub>P and graphene-based layers compared to the separated constituents.

The existence of nitrogen atoms led to the stability of doped sheets at greater total energies compared to their intact forms throughout the optimization. While the absolute atomic conformations of Ni<sub>2</sub>P/graphene achieve the binding energy at  $-2.64$  eV, a binding energy value of  $-2.96$  eV was obtained for their nitrogen-doped equivalent (Ni<sub>2</sub>P/NG). The molecular motion and the electronic structure are also affected by this greater value of bonding energy by boosting the kinetic energy of the doped system. Any system with the least feasible energy represents the optimized structure to attain steady energy configuration.

### 3.2. Projected density of states and band structure

The projected density of states (PDOS) was employed to analyze the electronic specifications of pure and diverse  $\text{Ni}_2\text{P}$  heterostructures. In the whole PDOS, the Fermi levels shifted to zero. Fig. 2a depicts the PDOS of the graphene monolayer. A Dirac point that can be seen at the Fermi level is the exclusive electronic zero bandgap representative of graphene, being both experimentally and theoretically related to the existing reports [57,58]. The two visible peaks at  $-1.85$  eV and  $2.22$  eV belong to the energy of the Highest Occupied Molecular Orbital (HOMO) and the Lowest Unoccupied Molecular Orbital (LUMO), respectively. These observations also agree with those reported in a previous study [59]. Fig. 2b illustrates the PDOS of the NG monolayer. The downshift of the Dirac point of the total system (pink line) is visible from the Fermi level and into the conduction band. Close to the Fermi level, it is mainly involved in the hybridization of N-2p states and C-2p states, along with a variety of other states that exist at the Fermi level and suggest more conductivity of the doped system than the intact graphene. The electronic specifications of doped nitrogen on graphene were further studied by calculating the band structure. Fig. 2a exhibits the energy band structure of intact graphene. Gamma, M, and K are the highly symmetrical points in the Brillouin zone that corresponds to the supercell.

At the K-points of undoped graphene, the bandgap is zero, and the conductive and valence bands are cone-shaped, in which the points of the cones touch at the Fermi energy. The zero value for the density of states is due to the cones touching at an indefinitely minor point (the Dirac point) without any 'range' or 'extent' in E-k space (i.e., states are absent in this point).

The band structure of NG in Fig. 2b indicates that the Fermi level is shifting upwards into the conduction band (with an N atom that has one more electron than a C atom) compared to that of intact graphene (as seen in Fig. 2a). These observations indicate that the material turns into n-type metallic due to nitrogen doping, and the role of the nitrogen atom is an n-type dopant. The band structures determined here for the intact and NG fully correspond to those reported previously [60–62].

According to the results shown in Fig. 2c, P-3p states have a strong hybridization with the Ni-3d ones at  $[-8.0$  eV,  $8.0$  eV], forming covalent bonds between them. The main composition of valence electrons of  $\text{Ni}_2\text{P}$  is the 3d orbitals of Ni atoms (Ni-3d), while the unoccupied electron above the Fermi level originates from the predominant Ni-3d orbitals and a minor number of P-3p orbitals (3p orbitals of P atoms). The distribution range of energy eigenvalues for the hybrid states is mostly  $0-2$  eV above the Fermi level. Additionally, Fig. 2c shows that Ni and P atoms are differentiated by PDOS at various locations. Additionally, more delocalization of the P-3p states of  $\text{Ni}_2\text{P}$  is seen with their much stronger resonance with Ni-3d states, indicating that the Ni–P bonds are more robust in

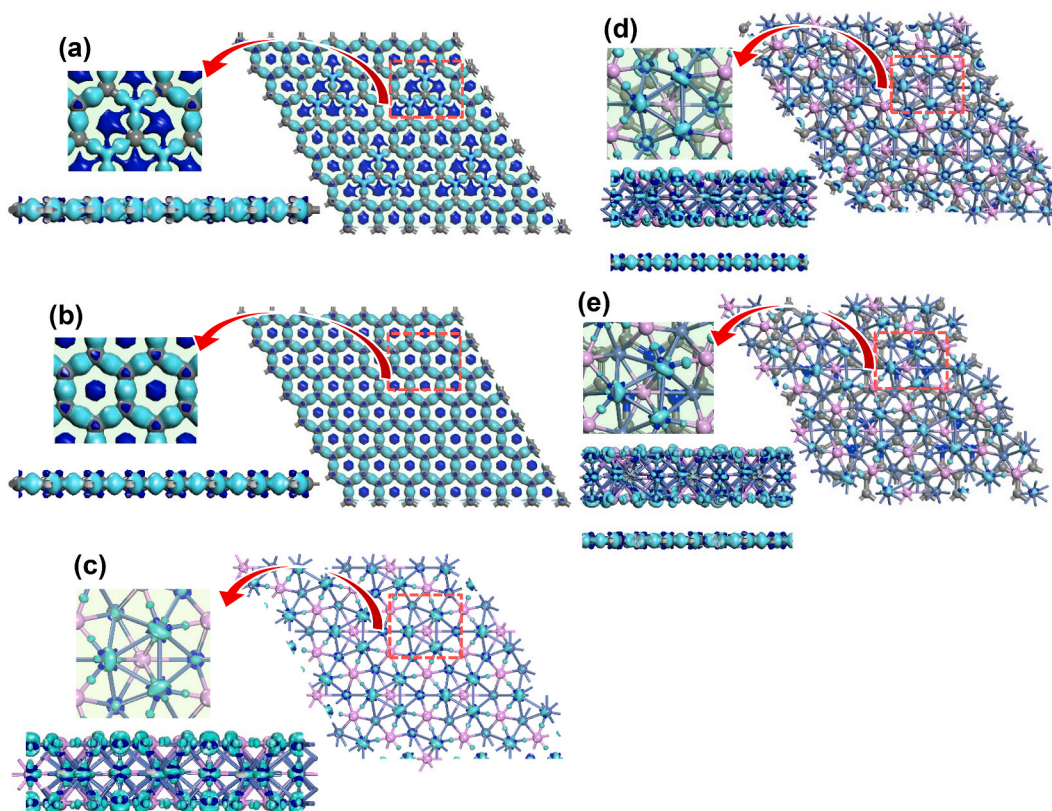


**Fig. 3.** The top and side views of the spatial mapping charge density difference ( $\Delta\rho$ ) profile of (a) Graphene monolayer, (b) N-doped graphene monolayer, (c) Pristine  $\text{Ni}_2\text{P}$ , (d)  $\text{Ni}_2\text{P}$ /graphene heterostructure, and (e)  $\text{Ni}_2\text{P}$ /NG heterostructure. The cyan and blue color isosurfaces display the accretion and depletion of electrons, in respective order, in which the isosurface value is set at  $0.05$   $e/\text{\AA}^3$ . (For interpretation of the references to color in this figure legend, the reader is referred to the Web version of this article.)

the Ni<sub>2</sub>P system.

In comparison to that of their constituents individually (Ni<sub>2</sub>P, graphene, and NG), electronic states increase exponentially for Ni<sub>2</sub>P/graphene and Ni<sub>2</sub>P/NG to values close to the Fermi level from the valence-electron states of C, N, P, and Ni (Fig. 2d and e). The C-2p orbitals of NG were dominant at the top of the valence band and the bottom of the conductance band of Ni<sub>2</sub>P/NG. The electrons of graphene or NG were easily transported to the Ni<sub>2</sub>P sheet. The condition of PDOSs for Ni<sub>2</sub>P/NG resembled that of Ni<sub>2</sub>P/graphene. A minor change has been observed in the intensity and shape of the PDOSs for both heterostructures, and no band gap was noticed.

The easy transmission of electrons from graphene and NG to the Ni<sub>2</sub>P sheet is highly possible. The electron was transmitted suitably due to the electron deficiency of the NG sheets. It can be concluded that the improved electrical conductance of composite structures of Ni<sub>2</sub>P and carbon-based materials is attributed to the electrical conducting graphene and NG itself. However, the calculated DFT in this study proves that the electronic structures of the two heterostructures are strongly affected by the coupled Ni<sub>2</sub>P and carbon-based materials, leading to the improved overall electrical conductance of the combined system. This helps efficiently transfer electrons across the VdW heterostructure, resulting in high reaction kinetics for the two heterostructures. Thus, the calculated DFT indicates the reasons for the far better electrochemical functionality of Ni<sub>2</sub>P/graphene and Ni<sub>2</sub>P/NG from the atomic-scale point of view.

### 3.3. Charge density difference and charge transfer

The electronic properties and the charge quantitatively transferred at the heterostructure interface (i.e., Ni<sub>2</sub>P/graphene and Ni<sub>2</sub>P/NG) were further investigated by examining the charge density and Hirshfeld charge population at the same adsorption sites, and the results illustrated in Fig. 3. The green and pink regions represent the charge depletion and accumulation.

The difference in the charge density of graphene and NG is shown in Fig. 3a and b. The electronegativity of carbon is 2.55, while that of nitrogen is 3.04 [63]. These findings correspond to the fact that electrons are denser around the nitrogen atom while the positive charge (green) is more concentrated around the C atoms than the N atom. These observations show that the charge-density difference influences the adsorption site of the H<sub>3</sub>O<sup>+</sup> ion due to nitrogen doping.

As depicted in Fig. 3c, the charge accumulation area (cyan color) nearly surrounds the Ni<sub>2</sub>P (Ni) sites, leading to the strong desorption of the adsorbed hydrogen on the Ni<sub>2</sub>P region.

Fig. 3d and e exhibit the charge-density difference for the heterostructures (i.e., Ni<sub>2</sub>P/graphene and Ni<sub>2</sub>P/NG). There is no overlapped electron orbital between Ni<sub>2</sub>P and graphene-based systems layers, suggesting poor VdW interaction between the layers of these heterostructures. These figures show the charge density change at the active surfaces following the heterostructure generation. Evidently, only the electronic density around the Ni region can be optimized by the hybrid structures. This shows that these atoms are the active sites for the HER, resulting in appropriate strong hydrogen adsorption and improving the HER catalytic activity.

**Table 1**

Hirshfeld charges analysis on the Ni<sub>2</sub>P, Ni<sub>2</sub>P/graphene, and Ni<sub>2</sub>P/NG structures for various positions of Ni (1–3) and P (4–9) atoms.

Position of different atomic charges on Ni <sub>2</sub> P sheet	1	2	3	4	5	6	7	8	9
Ni <sub>2</sub> P	-0.03	-0.03	-0.03	0.05	0.05	0.06	0.05	0.05	0.05
Ni <sub>2</sub> P/graphene	-0.04	-0.03	-0.04	0.06	0.05	0.06	0.06	0.06	0.06
Ni <sub>2</sub> P/NG	-0.05	-0.05	-0.02	0.06	0.06	0.05	0.04	0.05	0.06



It is clear from Fig. 3d and e that the charge accumulation area (cyan color) at the Ni site in the hybrid structures significantly shifts downward, and the equivalent charge depletion area (blue color) grows greater than that of the Ni site in Ni<sub>2</sub>P. This suggests that the positivity of the energy barrier of the Ni site further increases with poorer hydrogen bonding.

The estimated charge transfer of the Ni<sub>2</sub>P layer corresponds to the total summation of the Hirshfeld charge populations of the Ni and P atoms, as reported in Table 1. The charge transfer from Ni<sub>2</sub>P to graphene-based systems and vice versa are indicated by positive and negative values, respectively. A negative charge of Ni<sub>2</sub>P was observed for all the composites. Otherwise stated, the charging tendency is to be transferred from graphene-based materials to Ni<sub>2</sub>P. The order of the charge transfer level was Ni<sub>2</sub>P/NG and Ni<sub>2</sub>P/graphene. The charge transfer values of −0.22 and −0.97e were obtained for Ni<sub>2</sub>P/graphene and Ni<sub>2</sub>P/NG, respectively. N-doping in graphene (N-doped graphene) is shown to favor the charge provision for all hybrid structures.

### 3.4. Adsorption energy

Equation (3) was employed to calculate the adsorption energy of H<sub>3</sub>O<sup>+</sup> as follows:

$$E_{ads} = E_{sur+adsorbate} - E_{sur} - E_{adsorbate} \quad (3)$$

In this equation,  $E_{ads}$  is the adsorption energy,  $E_{sur+adsorbate}$  is the total energy of the surface-adsorbate(s) system,  $E_{sur}$  is the total energy of the surface, and  $E_{adsorbate}$  is the total energy of the separated adsorbate(s) with structural optimization in the gaseous phase. It is worth mentioning that the energy of dual dipole interplay arising from the limited size of the supercell is not corrected due to its minuscule value [64]. The configurations with the utmost stability following fully relaxed H<sub>3</sub>O<sup>+</sup> adsorption on pristine Ni<sub>2</sub>P, Ni<sub>2</sub>P/graphene, and Ni<sub>2</sub>P/NG are presented in Table 2. The distance between a particular atom of the adsorbate and the closest C atom on the Ni<sub>2</sub>P surface was determined from the output file position data, and a shorter distance indicated stronger adsorption. The O–H bond lengths and the H–O–H angle of 0.989 Å and 110.4° were obtained for the separated H<sub>3</sub>O<sup>+</sup> molecule, respectively. The adsorption energy for the diverse structures is also listed in Table 2, indicating negative adsorption energies for all structures. The higher negative adsorption value of Ni<sub>2</sub>P/NG suggests that H<sub>3</sub>O<sup>+</sup> molecules are more favorable to absorb on the surface of N-doped graphene compared to the Ni<sub>2</sub>P/graphene and pristine Ni<sub>2</sub>P.

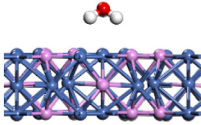
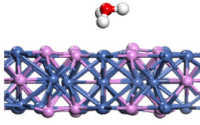
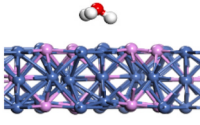
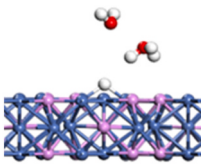
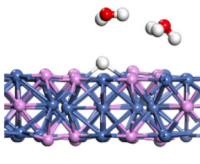
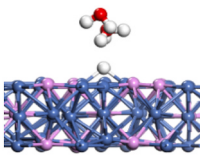
### 3.5. Reaction pathway of the hydrogen evolution reaction

#### 3.5.1. Volmer reaction

Two types of possible pathways are recommended to reduce protons to hydrogen in the HER mechanism in an acidic medium, including the Volmer-Heyrovsky or the Volmer-Tafel mechanism [65,66]. The primary electrochemical reaction (i.e., Volmer reaction) denotes the initially adsorbed protons (H<sup>+</sup>) from the acid solution for forming adsorbed hydrogen (Equation (4)). The Volmer-Heyrovsky mechanism includes the reaction of H<sup>+</sup> produced from water splitting with one adsorbed surface hydrogen (H<sub>ads</sub>) to form molecular hydrogen H<sub>2</sub> (Equation (5)). The Volmer-Tafel mechanism, however, includes reacting two numbers of H<sub>ads</sub> with one another to form H<sub>2</sub> (Equation (6)). The total reaction rate is controlled by the rate of the most sluggish step [67,68].



**Table 2**  
Adsorption energy of hydronium over various catalysts.

Catalyst	Ni <sub>2</sub> P	Ni <sub>2</sub> P/graphene	Ni <sub>2</sub> P/NG
Configuration			
Adsorption Energy (eV)	−0.187	−0.204	−0.210
Configuration			
4	−0.180	−0.185	−0.188





According to previous reports [69–71], the HER catalytic activity of a catalyst has an association with the kinetic energy barrier of the hydrogen evolution pathway. To understand the graphene and NG impacts on the catalytic HER activity, the in-depth HER pathway on the Ni<sub>2</sub>P, Ni<sub>2</sub>P/graphene, and Ni<sub>2</sub>P/NG catalysts was further examined by DFT calculations.

The simple steps of the Volmer reaction for the pristine Ni<sub>2</sub>P were studied to compare it with its bilayer systems. Fig. 4 schematically represents the initial (IS), transition (TS), and final (FS) states of the dissociation of hydronium ion on the surfaces of Ni<sub>2</sub>P, Ni<sub>2</sub>P/graphene, and Ni<sub>2</sub>P/NG. First, an H atom was located on the central hollow region of the Ni atom and above a P atom of Ni<sub>2</sub>P and hybrid slabs. The calculated energy barrier values were 0.27, 0.23, and 0.18 eV for the transition state on the Ni<sub>2</sub>P, Ni<sub>2</sub>P/graphene, and Ni<sub>2</sub>P/NG, respectively. The calculated interacting Ni–H bond distances were respectively 1.611 Å, 1.687 Å, and 1.760 Å at Ni<sub>2</sub>P, Ni<sub>2</sub>P/graphene, and Ni<sub>2</sub>P/NG surfaces, respectively. This suggests the slight weakness of the Ni–H bonds of the adsorbed species after their adsorption on the heterostructure surfaces. Table 2 clearly indicates the lower adsorption energy of the H<sub>3</sub>O<sup>+</sup> molecule on the surfaces of Ni<sub>2</sub>P/graphene and Ni<sub>2</sub>P/NG individually, in absolute value, than the energy needed for hydronium dissociation. This suggests slow kinetics for the primary Volmer step in the HER over the Ni<sub>2</sub>P catalyst; consequently, a high overpotential is required for the dissociation.

### 3.5.2. Tafel reaction

The Volmer-Tafel pathway was also calculated for the developed structures to investigate the reaction mechanism, illustrated in Fig. 5. The 2nd hydrogen atom was adsorbed on the Ni(II) site of Ni<sub>2</sub>P, Ni<sub>2</sub>P/graphene, and Ni<sub>2</sub>P/NG with mean bond lengths of 1.631, 1.630, and 1.625 Å for H–Ni(II) and adsorption energy values of 0.180, 0.185, and 0.188 eV, respectively. The energy barriers of 0.40, 1.12, and 0.28 eV with reaction energy values of –1, –1.23, and –1.24 eV on Ni<sub>2</sub>P, Ni<sub>2</sub>P/graphene, and Ni<sub>2</sub>P/NG, correspondingly, are involved in the H migration. This endothermic Tafel step has reaction energy values of 0.63, 0.85, and 0.94 eV, and the energy barrier values are 2.67, 2.47, and 1.89 eV for Ni<sub>2</sub>P, Ni<sub>2</sub>P/graphene, and Ni<sub>2</sub>P/NG, respectively. The desorption of the evolved H<sub>2</sub> molecule from the surface occurs in the FS, and the H–H bond length is 0.753 Å for the entire structure.

The reported observations generally demonstrate that the catalytic activity of Ni<sub>2</sub>P/NG is greater than that of the equivalent hybrid catalyst with no N introduction and pristine Ni<sub>2</sub>P. It is concluded that the present findings of calculations correspond to those obtained experimentally [41,72]. The greater HER catalytic activity of the heterostructures is attributable to the outstanding migratory capacity of the adsorbed single H atom and the lower energy barrier to forming H<sub>2</sub> following the introduction of graphene or NG into the Ni<sub>2</sub>P

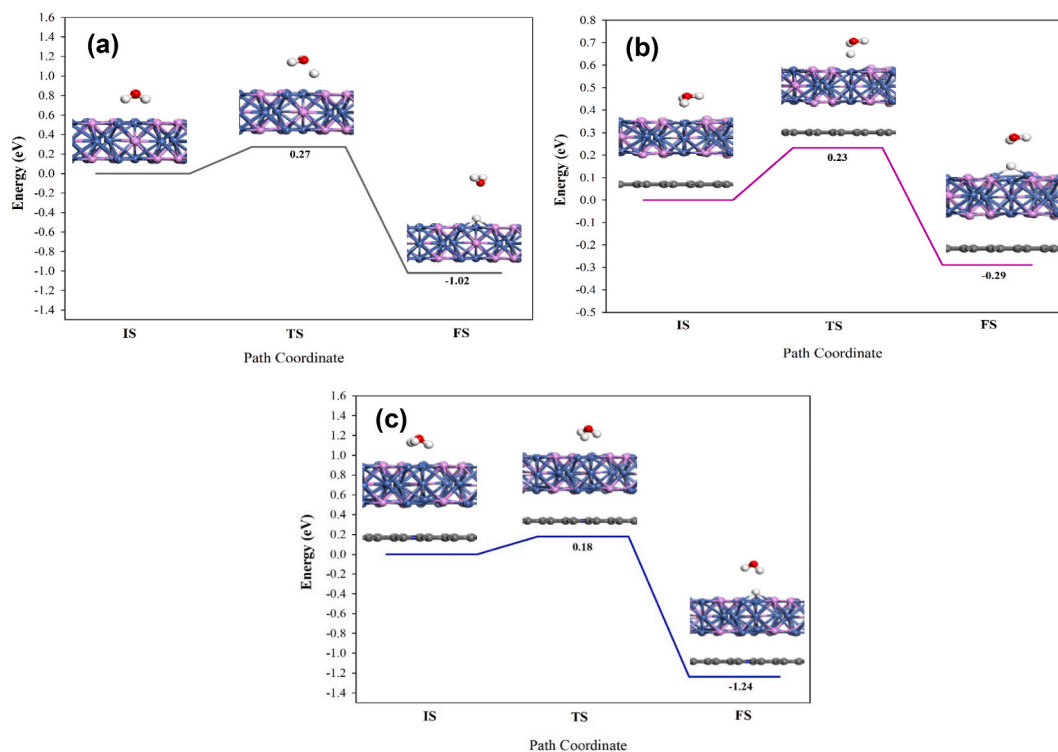


**Fig. 4.** The side view of the IS, TS, and FS structures are shown by the estimated MEPs of the Volmer reaction on (a) Pristine Ni<sub>2</sub>P, (b) Ni<sub>2</sub>P/graphene heterostructure, and (c) Ni<sub>2</sub>P/NG heterostructure, in which a white ball represents the transported H to the surface at the final state.

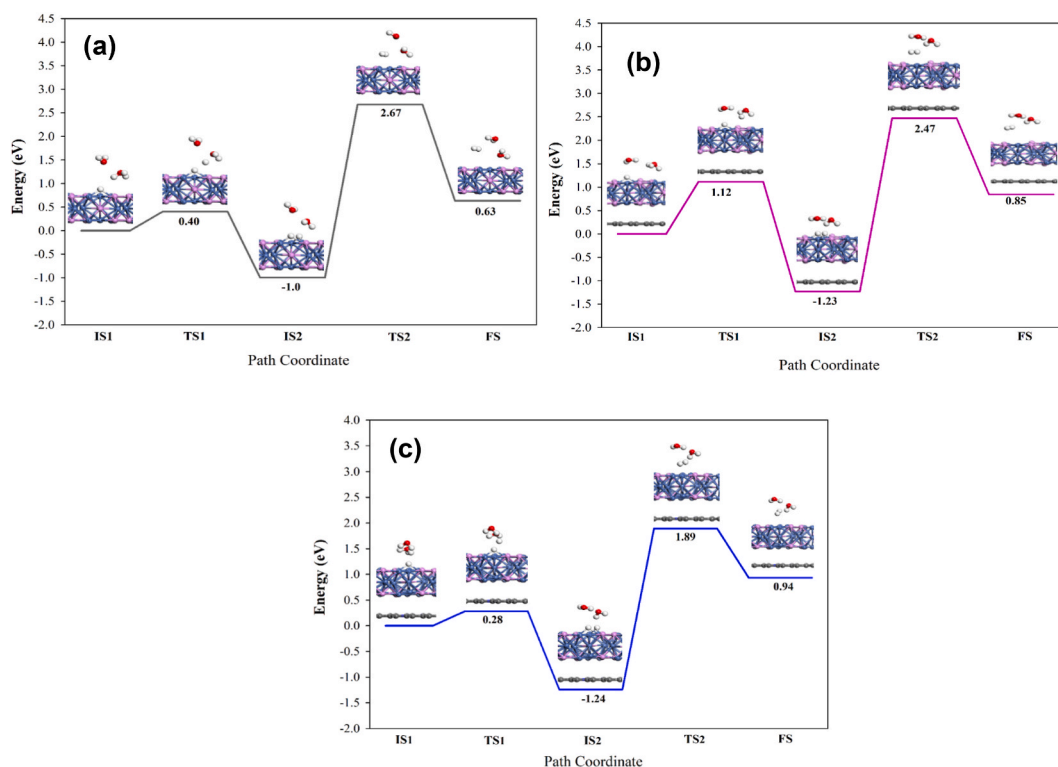


**Fig. 5.** Estimated MEPs for the Tafel reaction between two adjoining protons adsorbed on Ni-I and Ni-II regions on (a) pristine Ni<sub>2</sub>P, (b) Ni<sub>2</sub>P/graphene heterostructure, and (c) Ni<sub>2</sub>P/NG heterostructure. Structural changes of these processes are shown on the upper panel.

system.

### 3.5.3. Heyrovsky reaction

**Fig. 6** illustrates the Heyrovsky reaction pathway when the H<sub>3</sub>O<sup>+</sup> ion is present. In the IS, the interfacial H atom couples at the Ni hollow site. This H atom partially escapes from the surface in the TS, while an H atom of a hydronium ion in the water layer reaches the surface, with a distance of 0.957 Å between the two interacting H atoms. The H<sub>2</sub> molecule is created in the FS and departs from the surface. In this exothermal Heyrovsky step, the reaction energy values are -0.20, -0.16, and -0.18 eV on Ni<sub>2</sub>P, Ni<sub>2</sub>P/graphene, and Ni<sub>2</sub>P/NG, respectively. For Ni<sub>2</sub>P, the calculated energy barrier was 2.56 eV, compared with the reduced values calculated for Ni<sub>2</sub>P/graphene (1.98 eV) and Ni<sub>2</sub>P/NG (1.79 eV).

### 3.5.4. Overall reaction

The energy barrier between the developed catalysts was compared by considering two primary steps. The Ni<sub>2</sub>P/graphene and Ni<sub>2</sub>P/NG systems act more efficiently in water splitting than pristine Ni<sub>2</sub>P. The energy barrier declines with the introduction of N-doping. It is clear from these values reported in this section that the NG systems act superior to the intact graphene system as catalysts for water splitting. Additionally, comparing the energy barriers for the Tafel and Heyrovsky reactions on the pristine Ni<sub>2</sub>P system indicates a remarkably lower energy barrier for the Volmer-Heyrovsky reaction than that for the Volmer-Tafel reaction. This is suggestive of a faster Volmer-Heyrovsky reaction and the major pathway of HER. Furthermore, the Volmer-Tafel reaction is the rate-determining step (RDS) in the overall reaction.

## 4. Conclusion

Using the DFT calculations, water splitting on pristine Ni<sub>2</sub>P, Ni<sub>2</sub>P/graphene, and Ni<sub>2</sub>P/NG was investigated systematically in this research. The relatively poor interaction of these heterostructures is attributed to VdW interaction. The calculated binding energy reveals the thermodynamic stability of the heterostructures. The estimated PDOS and band structures indicate more conductivity of NG than intact graphene, being helpful in the water-splitting reaction. According to the charge density difference and the Hirshfeld analysis of composites, it was clear that the charge was transferred from the graphene or NG to Ni<sub>2</sub>P. The water splitting efficiency was estimated by initial calculation of the adsorption energy of a single hydronium ion on the developed catalyst surfaces, and the bond length and angle were calculated afterward. Graphene and NG enhanced water absorption on the Ni<sub>2</sub>P surface, as indicated by more negative adsorption energies and shorter bond lengths of carbon-based catalysts than pristine Ni<sub>2</sub>P. Eventually, the MEP of the

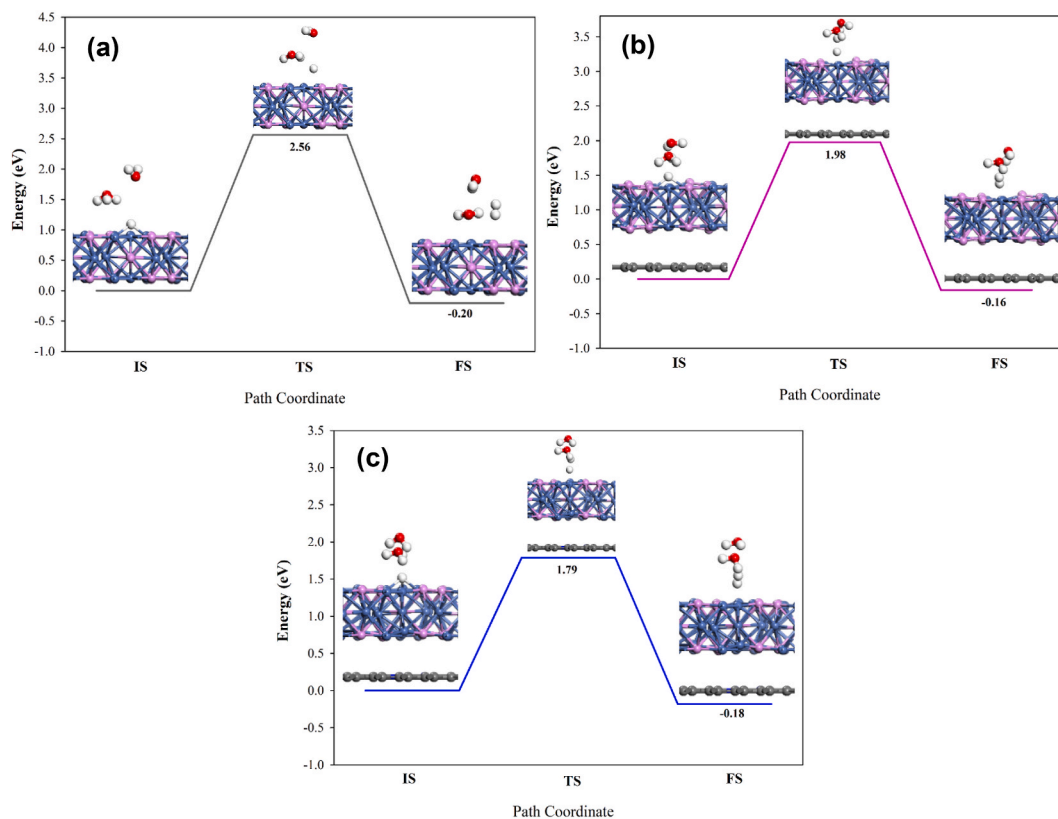


**Fig. 6.** Estimated MEPs for the Heyrovsky reaction between a proton adsorbed on a Ni–I site and a hydronium in solution on (a) Pristine Ni<sub>2</sub>P; (b) Ni<sub>2</sub>P/graphene heterostructure; and (c) Ni<sub>2</sub>P/NG heterostructure. The side panel shows alterations in the structures of these procedures.

adsorption of two hydronium ions was examined on the intact and NG. For water splitting, the Ni<sub>2</sub>P/NG catalyst presented lower barrier energy than Ni<sub>2</sub>P/graphene and pristine Ni<sub>2</sub>P. A comparison of the energetics for the Volmer, Tafel, and Heyrovsky reaction stages engaged in the HER mechanism reveals a rather energy barrier for the Tafel reaction than the Heyrovsky reaction. This indicates that the Volmer–Heyrovsky mechanism is the predominant reaction pathway; therefore, the Volmer–Tafel reaction is the RDS of the HER.

#### CRediT authorship contribution statement

**Amin Esmaeili:** Software, Supervision, Writing – original draft, Writing – review & editing. **Farhad Keivanimehr:** Formal analysis, Investigation, Resources, Software, Writing – original draft, Writing – review & editing. **Maryam Mokhtarian:** Data curation, Formal analysis, Funding acquisition, Investigation, Resources, Writing – original draft, Writing – review & editing. **Sajjad Habibzadeh:** Conceptualization, Methodology, Project administration, Supervision, Writing – original draft, Writing – review & editing. **Otman Abida:** Conceptualization, Methodology, Resources, Supervision, Writing – original draft, Writing – review & editing. **Mohammadreza Moghaddamian:** Data curation, Funding acquisition, Project administration, Validation, Visualization, Writing – original draft, Writing – review & editing.

#### Declaration of competing interest

The authors declare that they have no known competing financial interests or personal relationships that could have appeared to influence the work reported in this paper.

#### Appendix A. Supplementary data

Supplementary data to this article can be found online at <https://doi.org/10.1016/j.heliyon.2024.e27133>.

## References

- [1] X. Xu, Y. Zhong, Z. Shao, Double perovskites in catalysis, electrocatalysis, and photo (electro) catalysis, *Trends Chem* 1 (2019) 410–424.
- [2] I. Roger, M.A. Shipman, M.D. Szymes, Earth-abundant catalysts for electrochemical and photoelectrochemical water splitting, *Nat. Rev. Chem* 1 (2017) 1–13.
- [3] L. Tao, M. Huang, S. Guo, Q. Wang, M. Li, X. Xiao, et al., Surface modification of NiCo<sub>2</sub>Te<sub>4</sub> nanoclusters: a highly efficient electrocatalyst for overall water-splitting in neutral solution, *Appl. Catal. B Environ.* 254 (2019) 424–431.
- [4] H. Fan, H. Yu, Y. Zhang, Y. Zheng, Y. Luo, Z. Dai, et al., Fe-doped Ni<sub>3</sub>C nanodots in N-doped carbon nanosheets for efficient hydrogen-evolution and oxygen-evolution electrocatalysis, *Angew Chemie Int Ed* 56 (2017) 12566–12570.
- [5] X. Hu, Z. Zhan, J. Zhang, I. Hussain, B. Tan, Immobilized covalent triazine frameworks films as effective photocatalysts for hydrogen evolution reaction, *Nat. Commun.* 12 (2021) 1–9.
- [6] H. Zou, G. Li, L. Duan, Z. Kou, J. Wang, In situ coupled amorphous cobalt nitride with nitrogen-doped graphene aerogel as a trifunctional electrocatalyst towards Zn-air battery driven full water splitting, *Appl. Catal. B Environ.* 259 (2019) 118100.
- [7] H. Wang, X. Xiao, S. Liu, C.-L. Chiang, X. Kuai, C.-K. Peng, et al., Structural and electronic optimization of MoS<sub>2</sub> edges for hydrogen evolution, *J. Am. Chem. Soc.* 141 (2019) 18578–18584.
- [8] M. Zeng, Y. Li, Recent advances in heterogeneous electrocatalysts for the hydrogen evolution reaction, *J. Mater. Chem. A* 3 (2015) 14942–14962.
- [9] H. Louis, O.J. Ikenyirimba, T.O. Unimuke, G.E. Mathias, T.E. Gber, A.S. Adeyinka, Electrolytic activity of metal encapsulated, doped, and engineered fullerene-based nanostructured materials towards hydrogen evolution reaction, *Sci. Rep.* 12 (2022) 1–21.
- [10] K. Gong, F. Du, Z. Xia, M. Durstock, L. Dai, Nitrogen-doped carbon nanotube arrays with high electrocatalytic activity for oxygen reduction, *Science* 323 (80) (2009) 760–764.
- [11] J. Xie, J. Zhang, S. Li, F. Grote, X. Zhang, H. Zhang, et al., Controllable disorder engineering in oxygen-incorporated MoS<sub>2</sub> ultrathin nanosheets for efficient hydrogen evolution, *J. Am. Chem. Soc.* 135 (2013) 17881–17888.
- [12] K.L. Zhou, Z. Wang, C.B. Han, X. Ke, C. Wang, Y. Jin, et al., Platinum single-atom catalyst coupled with transition metal/metal oxide heterostructure for accelerating alkaline hydrogen evolution reaction, *Nat. Commun.* 12 (2021) 1–10.
- [13] M. Li, K. Duanmu, C. Wan, T. Cheng, L. Zhang, S. Dai, et al., Single-atom tailoring of platinum nanocatalysts for high-performance multifunctional electrocatalysis, *Nat. Catal.* 2 (2019) 495–503.
- [14] J. Li, G. Wei, Y. Zhu, Y. Xi, X. Pan, Y. Ji, et al., Hierarchical NiCoP nanocone arrays supported on Ni foam as an efficient and stable bifunctional electrocatalyst for overall water splitting, *J. Mater. Chem. A* 5 (2017) 14828–14837.
- [15] Y. Lian, H. Sun, X. Wang, P. Qi, Q. Mu, Y. Chen, et al., Carved nanoframes of cobalt–iron bimetal phosphide as a bifunctional electrocatalyst for efficient overall water splitting, *Chem. Sci.* 10 (2019) 464–474.
- [16] M.A. Khan, H. Zhao, W. Zou, Z. Chen, W. Cao, J. Fang, et al., Recent progresses in electrocatalysts for water electrolysis, *Electrochem. Energy Rev.* 1 (2018) 483–530.
- [17] S.D. Ghadge, O.I. Velikokhatnyi, M.K. Datta, P.M. Shanthi, P.N. Kumta, Computational and experimental investigation of Co and S-doped Ni<sub>2</sub>P as an efficient electrocatalyst for acid mediated proton exchange membrane hydrogen evolution reaction, *Catal. Sci. Technol.* 11 (2021) 861–873.
- [18] W. Zhou, J. Jia, J. Lu, L. Yang, D. Hou, G. Li, et al., Recent developments of carbon-based electrocatalysts for hydrogen evolution reaction, *Nano Energy* 28 (2016) 29–43.
- [19] X. Ma, G. Ning, C. Qi, C. Xu, J. Gao, Phosphorus and nitrogen dual-doped few-layered porous graphene: a high-performance anode material for lithium-ion batteries, *ACS Appl. Mater. Interfaces* 6 (2014) 14415–14422.
- [20] C. Wang, Y. Zhou, L. Sun, P. Wan, X. Zhang, J. Qiu, Sustainable synthesis of phosphorus-and nitrogen-co-doped porous carbons with tunable surface properties for supercapacitors, *J. Power Sources* 239 (2013) 81–88.
- [21] H.B. Wang, T. Maiyalagan, X. Wang, *ACS Catal.* 2 (2012) 781. CrossRef [CAS] Web Sci Times Cited n.d.;733.
- [22] Y. Zhao, R. Nakamura, K. Kamiya, S. Nakanishi, K. Hashimoto, Nitrogen-doped carbon nanomaterials as non-metal electrocatalysts for water oxidation, *Nat. Commun.* 4 (2013) 1–7.
- [23] K. F. du Gong, Z. Xia, M. Durstock, L.M. Dai, *Science* 323 (80) (2009) 760.
- [24] L. Qu, Y. Liu, J.-B. Baek, L. Dai, Nitrogen-doped graphene as efficient metal-free electrocatalyst for oxygen reduction in fuel cells, *ACS Nano* 4 (2010) 1321–1326.
- [25] Y. Zheng, Y. Jiao, Y. Zhu, L.H. Li, Y. Han, Y. Chen, et al., Hydrogen evolution by a metal-free electrocatalyst, *Nat. Commun.* 5 (2014) 1–8.
- [26] F. Lyu, S. Zeng, Z. Jia, F.-X. Ma, L. Sun, L. Cheng, et al., Two-dimensional mineral hydrogel-derived single atoms-anchored heterostructures for ultrastable hydrogen evolution, *Nat. Commun.* 13 (2022) 1–12.
- [27] K.S. Novoselov, o A. Mishchenko, o A. Carvalho, A.H.C. Neto, 2D materials and van der Waals heterostructures, *Science* (80-) (2016) 353.
- [28] Y. Liu, N.O. Weiss, X. Duan, H.-C. Cheng, Y. Huang, X. Duan, Van der Waals heterostructures and devices, *Nat. Rev. Mater.* 1 (2016) 1–17.
- [29] H. Li, K. Yu, C. Li, Z. Tang, B. Guo, X. Lei, et al., Charge-transfer induced high efficient hydrogen evolution of MoS<sub>2</sub>/graphene cocatalyst, *Sci. Rep.* 5 (2015) 18730.
- [30] P.T. Araujo, M. Terrones, M.S. Dresselhaus, Defects and impurities in graphene-like materials, *Mater. Today* 15 (2012) 98–109.
- [31] J. Shi, R. Tong, X. Zhou, Y. Gong, Z. Zhang, Q. Ji, et al., Temperature-Mediated selective growth of MoS<sub>2</sub>/WS<sub>2</sub> and WS<sub>2</sub>/MoS<sub>2</sub> vertical stacks on Au foils for direct photocatalytic applications, *Adv Mater* 28 (2016) 10664–10672.
- [32] R.K. Biroju, S. Pal, R. Sharma, P.K. Giri, T.N. Narayanan, Stacking sequence dependent photo-electrocatalytic performance of CVD grown MoS<sub>2</sub>/graphene van der Waals solids, *Nanotechnology* 28 (2017) 85101.
- [33] S. Bawari, N.M. Kaley, S. Pal, T.V. Vineesh, S. Ghosh, J. Mondal, et al., On the hydrogen evolution reaction activity of graphene–hBN van der Waals heterostructures, *Phys. Chem. Chem. Phys.* 20 (2018) 15007–15014.
- [34] Y. Shi, H. Zhang, W.-H. Chang, H.S. Shin, L.-J. Li, Synthesis and structure of two-dimensional transition-metal dichalcogenides, *MRS Bull.* 40 (2015) 566–576.
- [35] G. Shi, Z. Fan, L. Du, X. Fu, C. Dong, W. Xie, et al., In situ construction of graphdiyne/CuS heterostructures for efficient hydrogen evolution reaction, *Mater. Chem. Front.* 3 (2019) 821–828.
- [36] Suryawanshi Up, U.V. Ghorpade, D.M. Lee, M. He, S.W. Shin, P.V. Kumar, et al., Colloidal Ni<sub>2</sub>P nanocrystals encapsulated in heteroatom-doped graphene nanosheets: a synergy of 0D@ 2D heterostructure toward overall water splitting, *Chem. Mater.* 33 (2020) 234–245.
- [37] R. Boppella, J. Tan, W. Yang, J. Moon, Homologous CoP/NiCoP heterostructure on N-doped carbon for highly efficient and pH-universal hydrogen evolution electrocatalysis, *Adv. Funct. Mater.* 29 (2019) 1807976.
- [38] K. Tu, D. Tranca, F. Rodríguez-Hernández, K. Jiang, S. Huang, Q. Zheng, et al., A novel heterostructure based on RuMo nanoalloys and N-doped carbon as an efficient electrocatalyst for the hydrogen evolution reaction, *Adv Mater* 32 (2020) 2005433.
- [39] G. Zhang, X. Zheng, Q. Xu, J. Zhang, W. Liu, J. Chen, Carbon nanotube-induced phase and stability engineering: a strained cobalt-doped WSe<sub>2</sub>/MWNT heterostructure for enhanced hydrogen evolution reaction, *J. Mater. Chem. A* 6 (2018) 4793–4800.
- [40] Y. Qin, H. Li, J. Lu, Y. Feng, F. Meng, C. Ma, et al., Synergy between van der waals heterojunction and vacancy in ZnIn<sub>2</sub>S<sub>4</sub>/g-C<sub>3</sub>N<sub>4</sub> 2D/2D photocatalysts for enhanced photocatalytic hydrogen evolution, *Appl. Catal. B Environ.* 277 (2020) 119254.
- [41] D. Ma, K. Meng, J. Ma, Z. Jia, Y. Wang, L. Liu, et al., The catalytic performance enhancement of Ni<sub>2</sub>P electrocatalysts for hydrogen evolution reaction by carbon-based substrates, *Int. J. Hydrogen Energy* 44 (2019) 31960–31968.
- [42] R. Kumar, D. Das, A.K. Singh, C<sub>2</sub>N/WS<sub>2</sub> van der Waals type-II heterostructure as a promising water splitting photocatalyst, *J. Catal.* 359 (2018) 143–150.
- [43] F. Keivanimehr, S. Habibzadeh, M. Mokhtarian, Enhanced product quality through hydrodesulfurization of pyrolysis gasoline over a mixed metal oxide catalyst: an experimental and DFT study, *Fuel* 317 (2022) 123458.
- [44] S.J. Clark, M.D. Segall, C.J. Pickard, P.J. Hasnip, M.I.J. Probert, K. Refson, et al., First principles methods using CASTEP, *Zeitschrift Für Krist Mater* 220 (2005) 567–570.



- [45] J.P. Perdew, K. Burke, M. Ernzerhof, Generalized gradient approximation made simple, *Phys. Rev. Lett.* 77 (1996) 3865.
- [46] S. Grimme, Semiempirical GGA-type density functional constructed with a long-range dispersion correction, *J. Comput. Chem.* 27 (2006) 1787–1799.
- [47] G. Henkelman, B.P. Uberuaga, H. Jónsson, A climbing image nudged elastic band method for finding saddle points and minimum energy paths, *J. Chem. Phys.* 113 (2000) 9901–9904.
- [48] C. Peng, H. Bernhard Schlegel, Combining synchronous transit and quasi-Newton methods to find transition states, *Isr. J. Chem.* 33 (1993) 449–454.
- [49] W. Beker, W.A. Sokalski, Bottom-up nonempirical approach to reducing search space in enzyme design guided by catalytic fields, *J Chem Theory Comput* 16 (2020) 3420–3429.
- [50] L. Hu, H. Chen, Assessment of DFT methods for computing activation energies of Mo/W-mediated reactions, *J Chem Theory Comput* 11 (2015) 4601–4614.
- [51] M.M. Alavijeh, S. Habibzadeh, K. Roohi, F. Keivanimehr, L. Naji, M.R. Ganjali, A selective and efficient precious metal-free electrocatalyst for chlorine evolution reaction: an experimental and computational study, *Chem. Eng. J.* 421 (2021) 127785.
- [52] A. Ambrosetti, P.L. Silvestrelli, Adsorption of rare-gas atoms and water on graphite and graphene by van der Waals-corrected density functional theory, *J. Phys. Chem. C* 115 (2011) 3695–3702.
- [53] C. Rajesh, C. Majumder, H. Mizuseki, Y. Kawazoe, A theoretical study on the interaction of aromatic amino acids with graphene and single walled carbon nanotube, *J. Chem. Phys.* 130 (2009) 124911.
- [54] L. Zhao, R. He, K.T. Rim, T. Schiros, K.S. Kim, H. Zhou, et al., Visualizing individual nitrogen dopants in monolayer graphene, *Science* 333 (80) (2011) 999–1003.
- [55] J. Zhang, Z. Wang, Z. Zhu, A density functional theory study on oxygen reduction reaction on nitrogen-doped graphene, *J. Mol. Model.* 19 (2013) 5515–5521.
- [56] Y.-K. Lee, S.T. Oyama, Bifunctional nature of a SiO<sub>2</sub>-supported Ni<sub>2</sub>P catalyst for hydrotreating: EXAFS and FTIR studies, *J. Catal.* 239 (2006) 376–389.
- [57] M. Dvorak, W. Oswald, Z. Wu, Bandgap opening by patterning graphene, *Sci. Rep.* 3 (2013) 1–7.
- [58] S. Grimme, J. Antony, S. Ehrlich, H. Krieg, A consistent and accurate ab initio parametrization of density functional dispersion correction (DFT-D) for the 94 elements H-Pu, *J. Chem. Phys.* 132 (2010) 154104.
- [59] W. Wang, Y. Zhang, C. Shen, Y. Chai, Adsorption of CO molecules on doped graphene: a first-principles study, *AIP Adv.* 6 (2016) 25317.
- [60] P. Rani, V.K. Jindal, Designing band gap of graphene by B and N dopant atoms, *RSC Adv.* 3 (2013) 802–812.
- [61] X. Zhou, C. Zhao, G. Wu, J. Chen, Y. Li, DFT study on the electronic structure and optical properties of N, Al, and N-Al doped graphene, *Appl. Surf. Sci.* 459 (2018) 354–362.
- [62] H.W. Lee, H.S. Moon, J. Hur, I.T. Kim, M.S. Park, J.M. Yun, et al., Mechanism of sodium adsorption on N-doped graphene nanoribbons for sodium ion battery applications: a density functional theory approach, *Carbon N Y* 119 (2017) 492–501.
- [63] S.S. Nishat, M.T. Islam, S. Ahmed, A. Kabir, Ab initio study of oxygen evolution reaction and hydrogen evolution reaction via water splitting on pure and nitrogen-doped graphene surface, *Mater. Today Commun.* 25 (2020) 101602.
- [64] O. Leenaerts, B. Partoens, F.M. Peeters, Adsorption of H<sub>2</sub>O, NH<sub>3</sub>, CO, NO<sub>2</sub>, and NO on graphene: a first-principles study, *Phys. Rev. B* 77 (2008) 125416.
- [65] H.K. Kim, H. Jang, X. Jin, M.G. Kim, S.-J. Hwang, A crucial role of enhanced Volmer-Tafel mechanism in improving the electrocatalytic activity via synergetic optimization of host, interlayer, and surface features of 2D nanosheets, *Appl. Catal. B Environ.* 312 (2022) 121391.
- [66] F. Keivanimehr, S. Habibzadeh, A. Baghban, A. Esmaili, A. Mohaddespour, A.H. Mashhadzadeh, et al., Electrocatalytic hydrogen evolution on the noble metal-free MoS<sub>2</sub>/carbon nanotube heterostructure: a theoretical study, *Sci. Rep.* 11 (2021) 1–9.
- [67] Y. Wang, W. Tian, J. Wan, W. Fu, H. Zhang, Y. Li, et al., Probing the origin of group VB transition metal monocarbides for high-efficiency hydrogen evolution reaction: a DFT study, *Appl. Surf. Sci.* 539 (2021) 148312.
- [68] W. Li, G. Liu, J. Li, Y. Wang, L. Ricardez-Sandoval, Y. Zhang, et al., Hydrogen evolution reaction mechanism on 2H-MoS<sub>2</sub> electrocatalyst, *Appl. Surf. Sci.* 498 (2019) 143869.
- [69] Y. Liu, R. Duan, X. Li, L. Luo, J. Gong, G. Zhang, et al., Unraveling the electronic effect of transition-metal dopants (M= Fe, Co, Ni, and Cu) and graphene substrate on platinum–transition metal dimers for hydrogen evolution reaction, *Inorg. Chem.* 61 (2022) 13210–13217.
- [70] N. Xue, Z. Lin, P. Li, P. Diao, Q. Zhang, Sulfur-doped CoSe<sub>2</sub> porous nanosheets as efficient electrocatalysts for the hydrogen evolution reaction, *ACS Appl. Mater. Interfaces* 12 (2020) 28288–28297.
- [71] Q. Tang, D. Jiang, Mechanism of hydrogen evolution reaction on 1T-MoS<sub>2</sub> from first principles, *ACS Catal.* 6 (2016) 4953–4961.
- [72] H. Zhang, W. Li, X. Feng, L. Zhu, Q. Fang, S. Li, et al., A chainmail effect of ultrathin N-doped carbon shell on Ni<sub>2</sub>P nanorod arrays for efficient hydrogen evolution reaction catalysis, *J. Colloid Interface Sci.* 607 (2022) 281–289.